Nuclear Engineering and Technology 52 (2020) 2290–2298

Contents lists available at ScienceDirect

Nuclear Engineering and Technology

journal homepage: www.elsevier.com/locate/net

Original Article

The bubble problem of the plasma facing material: A finite element study

Xiaoyan Kang [a, b], Xiyue Cheng [a], Shuiquan Deng [a, *]

[a] State Key Laboratory of Structural Chemistry, Fujian Institute of Research on the Structure of Matter, Chinese Academy of Sciences, Fuzhou, Fujian, 350002, PR China
[b] College of Chemistry, Fuzhou University, Fuzhou, Fujian, 350108, PR China

ARTICLE INFO

Article history:
Received 11 November 2019
Received in revised form
13 February 2020
Accepted 19 March 2020
Available online 24 March 2020

Keywords:
Finite elements analysis
First wall material
Bubble
Damage evaluation
Stress concentration

ABSTRACT

The damage of first wall material in fusion reactor due to the bubbles caused by plasma has been studied by introducing a relation between the von Mises equivalent stress and the temperature field. The locations and shapes of the bubbles and the synergetic effect between the different bubbles under steady operational conditions have been studied using the finite elements method. Under transient heat loads, plastic deformations have been found to occur, and are significantly enhanced by the presence of the bubbles. The calculated concentration locations of von Mises equivalent stress are well consistent with the observed crack positions of the tungsten surface in many test experiments. Our simulations show that the damage of the bubbles is not severe enough to lead to catastrophic failure of the tungsten armor; however, it can cause local and gradual detachment of tungsten surface, which provides a reasonable explanation for the observed pits and rough or hairy surface morphology etc. Considering the transient heat loads, the lower bound of the security thickness of the tungsten tile is estimated to be greater than 2 mm.

1. Introduction

Tungsten has the highest melting point, a good thermal conductivity and a low sputtering rate, and hence has been chosen as a plasma facing material for the first wall and diverter in the International Thermonuclear Experimental Reactor (ITER) project [1–7]. As a plasma facing material, tungsten is exposed to extremely high fluxes of high energy particles such as helium (He) and hydrogen (H), which leads to the formation of gas bubbles and severe damages at the surface, and thus the reduction of the life span of the materials [8–11]. Many voids or bubbles at the length scale of tens of micrometers in tungsten have already been observed in some test experiments [12,13]. Many theoretical studies examined the nucleation and growth mechanism of the bubbles in tungsten [14]. Liu et al. [15] considered the microscopic vacancy trapping mechanism for the formation of H bubble in W by investigating the energetics of H-vacancy interaction and the kinetics of H segregation with first-principles method. You et al. [16] studied the influence of hydrogen- or helium-atom clustering on the vacancy evolution in tungsten with calculations based on density functional theory (DFT). The role of the helium-atom clustering problem in inducing the blistering in tungsten was studied by Henriksson et al. [17,18] using molecular dynamics (MD) method. Juslin et al. [19] developed new tungsten-helium interatomic potentials to simulate the He bubble formation and to determine the formation energies, the ground state positions of He point defects and the self-interstitial atoms in tungsten. However, the model bubbles used in these theoretical simulations are much smaller in size than the actual bubbles observed in the test experiments.

Recently, the gas bubble and crack problems have also been studied by using the finite elements method on a macro-scale [20–22], which focus on the early stage of the blister-formation process due to the high pressure of gas thereby explaining a part of the experimental phenomena. In all these simulations, the thermal stress caused by the plasma and other high energy particles such as neutrons is neglected. These simplifying approximations result in inconsistency between the simulated results and the experimentally observed facts concerning the cracking of the bubbles and their coalescence [21,23,24]. To remedy this situation, it is necessary to evaluate tungsten as a first wall material by taking the effect of thermal stress into consideration. On the basis of the

* Corresponding author.
E-mail address: sdeng@fjirsm.ac.cn (S. Deng).

https://doi.org/10.1016/j.net.2020.03.020

finite elements method, we carried out our theoretical studies on the gas bubble problem of tungsten under steady operational conditions and transient heat loads using a new thermal-stress coupled model. In the following we report the results of our analysis.

2. Models and calculation methods

2.1. Models

A tungsten tile on the first wall is normally designed to have a thin slab shape, which has a dimension of tens of millimeters in length and width, and about several millimeters in thickness. In some test experiments, both round and ellipsoidal bubbles with sizes of a few to tens of micrometers have been observed to locate in the interior or near the surface of the tungsten sample [12,13]. Taking into account these results, a thin cuboid model with a size of $50 \times 50 \times 2$ mm^3 was built for all simulations (see Fig. 1). Throughout this work, a Cartesian coordinate system with the origin chosen at the center of the model is used (Fig. 1). The damage effects caused by gas bubbles are then studied under steady operational and transient heat loads conditions.

The heat conduction process is described by the energy conservation equation [25],

$$\rho C_p \frac{\partial T}{\partial t} = \nabla(k\nabla T) + Q \tag{1}$$

where ρ, C_p and k are the density, the specific heat and the thermal conductivity of a material, respectively. Q in Eq. (1) represents the heat generation rate per volume. The volumetric heating in the first wall of the ITER working conditions is designed to be ~ 15 MW/m^3 [26], which is used throughout this work. Eq. (1) can be solved under different boundary conditions corresponding to the actual situations.

2.2. Boundary conditions

In this work, we use two types of boundary conditions, which amount to a source of heat on the surface caused by the plasma irradiations (or neutron wall load) and by a cooling device. The boundary condition for the plasma irradiations is described by

$$\mathrm{n}(-k\nabla T) = -q_0 \quad atz = 1mm \tag{2}$$

where q_0 (in units of W/m^2) is the value of heat flow from the plasma, the minus sign indicates the inward heat flow direction, and **n** is the outward normal vector of the top surface. For the steady working condition, $q_0 = 1.0$ MW/m^2 is chosen, which is slightly larger than the designed technological value of the ITER [3,26]. The boundary condition for the cooling device is described by

$$\mathrm{n}(-k\nabla T) = h(T_s - T_{ext}) atz = -1mm \tag{3}$$

where h is the heat transfer coefficient (in W/m^{2}K), T_s is the surface temperature of the tungsten tile, and T_{ext} is the temperature (K) of the coolant. For the other four small boundary surfaces, the heat-insulating condition (i.e., $q_0 = 0$) is assumed in Eq. (2). This is a good approximation because the tungsten tiles are separated from each other by ditches and because they have a very small surface area. Besides, the inner surfaces of the bubble are assumed as insulated boundaries as the gas conductivity inside the bubble is considerably low compared with tungsten. With these boundary conditions, Eq. (1) can be solved to obtain the scalar temperature field $T(r,t)$ in our model. The time dependence disappears for the steady state case. The parameters for the coolant used in this work are $T_{ext} = 100$ °C as given in the ITER standard [26], and $h = 3000$ W/m^{2}K used in earlier studies [27]. In addition, the bottom side of the tungsten tile model is assumed to be fixed, which implies the following boundary condition for the displacement in solving the stress-strain constitutive equations,

$$u_z|_{z=-1mm} = 0 \tag{4}$$

where u_z is the z-direction component of the displacement vector $\boldsymbol{u}$, while the others are assumed to be free.

2.3. The von mises (vMES) criterion and the maximum vMES problem under thermal load

The von Mises equivalent stress (vMES) σ_e is defined as follows,

$$\begin{aligned}\sigma_e &= \sqrt{\frac{3}{2}\sum_{i,j=1}^{3}\left[\sigma_{ij} - \frac{1}{3}(\sigma_{11}+\sigma_{22}+\sigma_{33})\right]^2} \\ &= \left(\frac{1}{2}\left[(\sigma_1-\sigma_2)^2 + (\sigma_2-\sigma_3)^2 + (\sigma_3-\sigma_1)^2\right]\right)^{1/2}\end{aligned} \tag{5}$$

where σ_1, σ_2, and σ_3 are the three principal stress components of the Cauchy stress tensor. The general definition of the vMES based on the components of the Cauchy stress tensor is simplified to Eq. (5), because it is independent of the coordinate system. The von Mises plasticity condition reads as follows.

$\sigma_e < \sigma_{ys}$ for no plasticity

$$\sigma_e \geq \sigma_{ys} \text{ for plasticity} \tag{6}$$

where σ_{ys} is a material parameter (i.e., the yield strength). The von Mises criterion has been widely used to describe the plastic transformation of metals. Throughout this work we will use it as a criterion to evaluate the damage effects of bubbles to the tungsten tile.

By definition, the vMES is a scalar field while σ_{ys} is only a scalar parameter. Thus, the judgment made using the von Mises criterion should be pointwise. This reduces the solution of the inequality, Eq. (6), to finding the locations where the vMES field takes maximum values. In engineering, similar locations are often called stress raisers, which include notch tips, slots, grooves, cracks, sharp corners, and holes [28]. The relevant phenomenon is termed the stress concentration, referring to the Cauchy stress tensor σ (quite often its primary component σ_i) under some simple mechanic loads. As can be seen from Eq. (5), the maximum vMES problem is connected

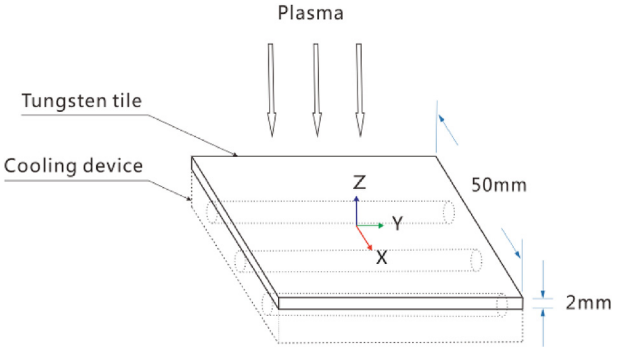

Fig. 1. A schematic diagram of the model used for simulating a tungsten tile (solid lines) together with a cooling base shown as tubes (dotted lines).

to that of the Cauchy primary stress tensor but not in a direct way. In this work we deal with heat load very different from those used in many classic studies [28], so we need to derive some new relations to explain the obtained numerical results.

Mathematically, the stress concentration at a point means that at least one component of a stress tensor, $\sigma_{ij}(\boldsymbol{r})$, takes a local maximum. The stress tensor is related to the elastic strain tensor as follows,

$$\{\sigma(\boldsymbol{r})\} = [\mathrm{D}]\{\varepsilon_{el}(\boldsymbol{r})\} \tag{7}$$

For an isotropic material, as in the current case, the stress tensor can be explicitly represented by using the Lamè constants (λ, μ) as follows [29],

$$\sigma_{ij} = \lambda\delta_{ij}\sum_{k}\varepsilon_{kk} + 2\mu\varepsilon_{ij} \;\; i,j,k = 1,2,3 \tag{8}$$

Eq. (8) indicates clearly that each off-diagonal component of the stress tensor is proportional to a unique shear component of the strain tensor. From Eq. (8), the following equation can be established to solve the extremal value problem of the shear component.

$$\nabla\sigma_{ij}(\boldsymbol{r}) = 2\mu\nabla\varepsilon_{ij}(\boldsymbol{r}), \;\; \text{for } i \neq j \tag{9}$$

For the diagonal stress component, we have the following more complicated relation,

$$\nabla\sigma_{ii}(\boldsymbol{r}) = \lambda\sum_{k}\nabla\varepsilon_{kk}(\boldsymbol{r}) + 2\mu\nabla\varepsilon_{ii}(\boldsymbol{r}) \tag{10}$$

These relations indicate that the stress concentration is completely dependent on the critical point of the strain components, though not necessarily on a specific component. The above relations can be expressed in a more concise form, if we use a composite function to express the definition of vMES as follows,

$$\sigma_e(\boldsymbol{r}) = \sigma_e\big(\sigma_{ij}(\varepsilon_{lm}(\boldsymbol{r}))\big) \tag{11}$$

In Eq. (11), the subindex *ij* and *lm* refer to the independent components of the Cauchy stress and elastic strain tensors, respectively. Assume that there is only one heat load as in the current situation. Then, before the setting in of plastic deformation, the elastic strain depends uniquely on the thermal strain. Thus, under the isotropic approximation, Eq. (11) can be written as follows,

$$\sigma_e(\boldsymbol{r}) = \sigma_e\big(\sigma_{ij}(\varepsilon_{th}(\boldsymbol{r}))\big) \tag{12}$$

The extremal value problem of vMES can be solved by taking the gradient of both sides of Eq. (12) as follows,

$$\nabla\sigma_e(\boldsymbol{r}) = \frac{\partial\sigma_e}{\partial\sigma_{ij}}\frac{\partial\sigma_{ij}}{\partial\varepsilon_{th}}\nabla\varepsilon_{th}(\boldsymbol{r}) \tag{13}$$

In Eq. (13) the Einstein summation convention for the sub-index ij was assumed, where ij runs over the independent components of the Cauchy stress tensor. Eq. (13) reduces the extremal value problem of vMES to that of thermal strain. In view of Eq. (13), we focus on the gradient of the thermal strain as shown below to explain our results.

$$\nabla\varepsilon_{th} = \alpha(T)\nabla T \tag{14}$$

In Eq. (14) the weak temperature dependence of the expansion coefficient α is neglected. Eq. (14) reduces the extremal value problem of thermal strain to that of temperature. We finally arrive at the following result,

$$\nabla\sigma_e(\boldsymbol{r}) = \frac{\partial\sigma_e}{\partial\sigma_{ij}}\frac{\partial\sigma_{ij}}{\partial\varepsilon_{th}}\alpha(T)\nabla T(\boldsymbol{r}) \tag{15}$$

The above expression indicates that the extremal value of vMES occurs at the same location as that of the temperature. Note that the maximum value of vMES depends not only on the variation of temperature around the extremal point but also on the local geometry. The critical condition, i.e., $\nabla T(\boldsymbol{r}) = 0$, is difficult to completely satisfy in practical situations, but can be partially met along a specific direction, e.g., $\frac{\partial}{\partial z}T(\boldsymbol{r}) = 0$.

In this work all calculations were carried out by using the ANSYS Workbench 12.0. A tetrahedral mesh is constructed automatically, while the region around the bubble is refined adaptively. Shown in Table 1 are the necessary physical parameters [30,31] used in this work.

3. Results and discussion

3.1. Steady state operation

3.1.1. Model without bubble

To evaluate the damage effects of gas bubbles, we have first simulated the tungsten tile without any damage under the thermal and displacement boundary conditions (Eqs. (2) and (3)). Shown in Fig. 2 is the calculated vMES field. The calculated maximum thermal deformation, 58.34 μm, occurs at the four corners of the top surface within the xy plane, while that along the z direction is only ~ 3.3 μm. This expansion mode has a very weak *z*-coordinate dependence, though the base plane is indeed a little less expanded (58.11 μm at each corner). The seemingly very different expansion within the xy plane and that along the z direction yet result in nearly identical strain, i.e., 0.165%, which indicates an isotropic expansion. It is obvious from Fig. 2 that the maximum vMES, 27.2 MPa, appears at the four corners of the base plane. As the model has a four-fold symmetry (C_{4v} point group symmetry), the four edges parallel to the x and y axes are equivalent, and so are the four corners. At each corner of the base plane, the largest component (26.68 MPa) of the primary stress tensor is σ_z, while the other two components (σ_{45° and σ_{-45°) along the two perpendicular diagonal directions (45° and -45°) are negligibly small. According to Eq. (5), the vMES is thus mainly contributed by the σ_z component with calculated compressive character. The maximum effective stress found at the corners is evidently a stress concentration phenomenon, since corner is a typical stress raiser [28]. As shown in Fig. 2, the principal stress on one edge of the basal plan parallel to the x axis has a very weak x-coordinate dependence. The calculated principal stresses remain almost unchanged around the value of (9.62, 0.53, −18.0) along x-axis, where the negative sign indicates a compressive character. With the principal stress the vMES value is calculated to be ~24.38 MPa for each of the basal plane. Comparing this value with that at the corners, it is clear that the stress concentration at an edge is not as effective as that at the corner. It should be noted that the thermal stress produced by the heat loading is isotropic, which is different from the cases of external uniaxial loads.

The above discussions suggest that the corners of the tungsten tiles had better be rounded to reduce the stress concentration, though it is not a big concern according to our simulations. The compressive character of the stress field has been revealed by the calculated largest primary stress components within the xy plane (e.g. $\sigma_{45^\circ} = \sigma_{-45^\circ} = -20.06$ MPa at the center) in the top surface. This result agrees very well with the experiments wherein the compressive stresses are found through the XRD data [32,33].

Table 1
Physical properties of tungsten.

	Symbol	Value
Density	ρ (kg/m^3)	19302.7−0.23786*T-2.2448*10^{-5}*T^2
Thermal conductivity	k (W/m K)	174.9274−0.1067*T+5.006710^{-5}*T^2-7.8349*10^{-9}*T^3
Specific heat capacity	C_p (J/kg K)	128.308 + 3.2797*10^{-2}*T-3.4097*10^{-6}*T^2
Expansion coefficient	α (10^{-6}K^{-1})	6.07*10^{-11}*T^3-1.47*10^{-7}*T^2+5.5*10^{-4}*T+4.43
Young's modulus	E (GPa)	397.903−2.3066*10^{-3}*T-2.7162*10^{-5}*T^2
Tangent modulus	E_T (GPa)	14.5
Poisson's ratio	ν	0.279 + 1.0893*10^{-5}*T
Yield strength	σ_{ys} (MPa)	1384.617−1.214*T+3.131*10^{-4}*T^2-1.896*10^{-8}*T^3 (20 °C < T < 2500 °C)

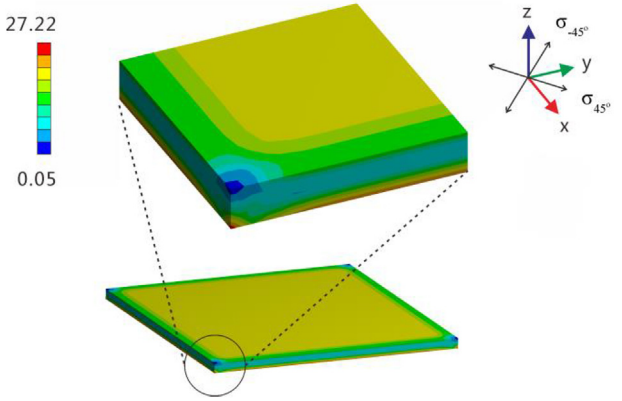

Fig. 2. Calculated vMES (in MPa) field on a model without bubble. For clarity, the local distribution of vMES around one corner is magnified. The color bar indicates the values of the calculated vMES field. (For interpretation of the references to color in this figure legend, the reader is referred to the Web version of this article.)

3.1.2. Simulation with a single bubble

The single bubble case was first studied with a round bubble of diameter 10 μm and centered at (0, 0, 990) μm in the coordinate system shown in Fig. 1, where the size of the bubble chosen is comparable with the average value of those observed in experiments (5–25 μm) [13]. The zenith of the round bubble is 5 μm below the top surface of the model. As shown in Fig. 3, the concentration of the vMES occurs in three regions around the bubble instead of the corners and edges of the no-bubble model.

The calculated values of the vMES near the zenith, the equator and the nadir of the bubble are around 35.4, 31.1 and 33.7 MPa, respectively, while that at each corner of the base plane is 18.8 MPa. This indicates that in the current case a bubble is a stronger stress

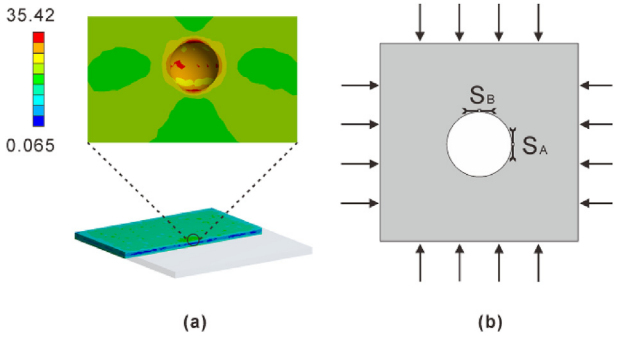

Fig. 3. (a) The calculated vMES distribution in part of the tungsten tile model, the local distribution around the bubble is magnified for clarity. (b) A sheet with a hole at the center, the biaxial external compressive loads are shown by arrows, while S_A and S_B represent the stress tangential to the equatorial and zenith point of the bubble, respectively.

concentrator than a corner. This follows more directly from the calculated largest primary stress components (~−40.6, ~ −39.3, ~ −26.8, for the zenith, the nadir and the equatorial regions, respectively). All these dominating components lie in the xy plane and show compressive character, while the z-component is about 1/8 (compressive) and 1/3 (tensile) of them for the pole and equatorial regions, respectively. Such a difference between the xy-plane and the z-axial components reflects the C_{4v} geometrical symmetry of the model (see Fig. 1) and the boundary conditions. The calculated largest primary stress components reveal a very different stress concentration character in comparison with some analytic results obtained for uniaxial or biaxial loading. For uniaxial case, it is understandable because the loading mode is too different. On the other hand, as our model can approximately be considered as a two dimensional one for its geometrical size (see Fig. 1) it seems to be comprehensible by resorting to the biaxial loading model [34]. However, according to the biaxial loading model the tangent stress component at the poles and the equator are both 2S with S being the loading stress in the x and y directions, respectively. With this model if one assumes two effective compressive loads as shown in Fig. 3b, the two nearly identical compressive stresses in the two pole regions can be explained. Nevertheless, the compressive tangent component at the equator (smaller in magnitude) remains unsolved. This disagreement reveals the essential difference between a thermal stress and a simple external mechanic loads. To understand these phenomena, we need to resort to Eq. (15).

In Fig. 4a, the temperature gradients along two lines in the direction of x-axis are shown together with their corresponding temperature distributions (see inset). It is clear that the critical points with $\frac{\partial}{\partial x}T(\boldsymbol{r})|_{x=0} = 0$ occurs for the lines $(x, y = 0, z = p)$, $995 \leq p \leq 1000$ mm which are parallel to x axis but are located at different positions $(z = p)$ from the zenith of the bubble up to the surface of the model. This result gives a numerical verification for Eq. (15) and thus well explains the vMES concentration around the zenith of a bubble shown in Fig. 3a.

The peak values of the temperature at the critical points ($x = 0$, $y = 0$, $z = p$) explain also the compressive character of the corresponding primary stress components, because the neighboring points tend to resist the expansion at the critical point. Shown in Fig. 4b are similar results for two lines along the z-axis but at different distances to the equatorial point for comparison. Fig. 4b shows that $\frac{\partial}{\partial z}T(\boldsymbol{r})|_{z=990} \neq 0$ for $y = 0$ and for $x = 5$ and 15 μm. In fact, this equatorial point is only an inflection point as shown in the inset. Similarly, we have also studied $\frac{\partial}{\partial x}T(\boldsymbol{r})|_{x=5}$ with $z = 990$ and $y = 0$, which shows no criticality at the equatorial point. These results indicate that a weaker stress concentration can happen at the equatorial point in comparison with that around the zenith point. This is consistent with that revealed by the calculated primary stress components at the relevant points and the vMES in Fig. 3a. In addition, the calculated peak values of the temperature distribution at the equatorial point along the x and y direction

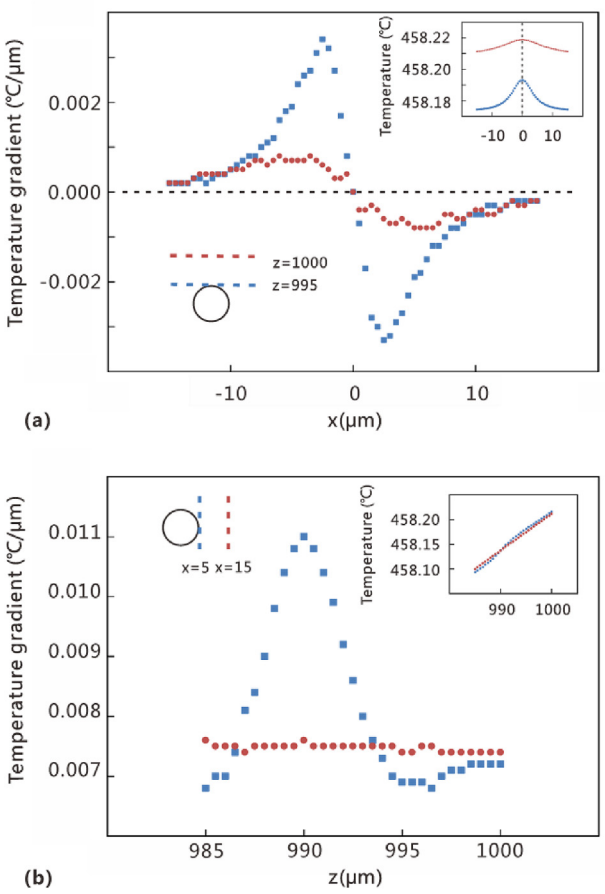

Fig. 4. (a) Temperature distribution and its gradient along two lines ($x, y = 0, z = 995$) and ($x, y = 0, z = 1000$) mm near the top of the bubble (see inset). (b) Temperature distribution and its gradient along two lines ($x = 5, y = 0, z$) and ($x = 15, y = 0, z$) near the equatorial point of the bubble (see inset). No critical point is found in this case.

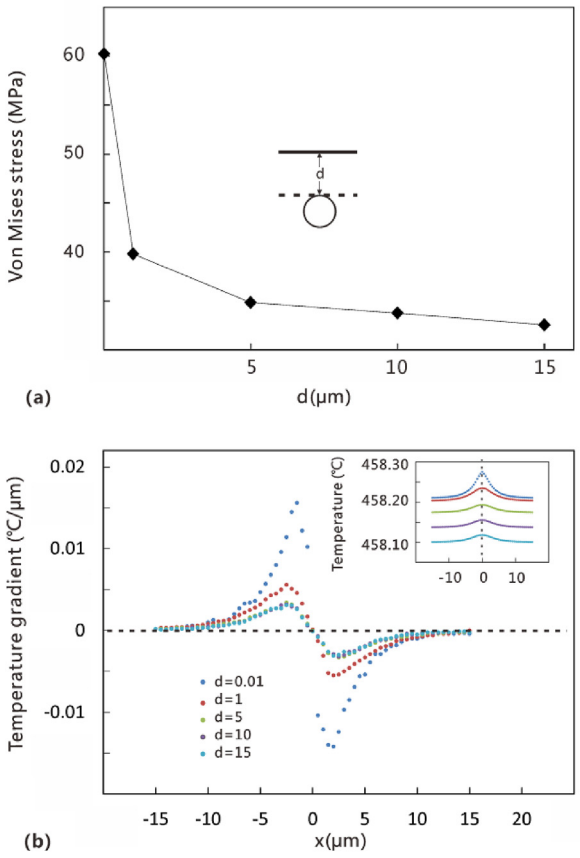

Fig. 5. (a) The dependence of the maximum vMES on the distance between the bubble zenith and the top surface of the tungsten tile model. (b) The temperature distribution along the lines ($x, y = 0, z = 999.99, 999, 995, 990, 985$) and the corresponding temperature gradients along the x direction.

(though marginally different) explain the compressive character of the primary stress components ($\sigma_x = -2.1$, $\sigma_y = -26.8$). In the z direction, as can be seen from the inset of Fig. 4b, the upper and the lower points induce tensile and compressive stresses, respectively, which together with the constraining force arising from the fixed boundary condition for the bottom surface complicate the analysis. Our simulation indicates that the upper point governs the situation, which leads to a tensile primary stress component $\sigma_z = 8.0$.

3.1.3. *The effect of the bubble location*

In the former section we have discussed the results of one single bubble located inside the tungsten tile. In the actual situations, a bubble may locate at different distances to the top surface of the model, which is expected to produce different stress concentrations and thus causing different damages to a tungsten tile. To assess this effect, we have simulated the one bubble problem at different distances to the top surface of the model. In Fig. 5a, the vMES at the zenith is shown as a function of d, the distance between the bubble zenith and the top surface.

As already shown in the last section ($d = 5$), the vMES attains the maximum value at the zenith for each case. As shown in Fig. 5a, the maximum value increases with the bubble approaching the top surface. The stress concentration as represented indirectly by vMES can be well explained by the similar arguments as used in the last section. As shown in Fig. 5b, the critical point of the temperature gradient lies exactly at the zenith of the bubble in each case. With the zenith approaching the top surface, the peak value of the temperature becomes more prominent so that the magnitude of the temperature gradient around the critical point becomes larger and larger. Our simulations indicate that the zenith of a bubble would be the weakest region where cracks or holes may develop. This has been unanimously confirmed by recent experiments [35–37] and MD simulations [38–40], which showed the rupture of bubbles near the surface.

In actual situation, bubbles may bulge out of the tungsten surface, which may be caused by high inner gas pressure inside a bubble [20]. To simulate this situation, we construct an oblate ellipsoid bubble with three semi-principal axes lengths chosen as 6, 6, 4 μm and 5, 5, 3 μm for the outer and inner surface, respectively. The c axis of the ellipsoid is chosen to be coincident with the z axis of the tungsten tile model (Fig. 1), while its center is chosen at (0, 0, 1000). The simulations performed under the steady-state operational conditions as described in part 2 results in the vMES distribution in the model as shown in Fig. 6a. The calculated maximum vMES, 24.73 MPa, lies at the intersection between the bubble and the tungsten surface, i.e., near the notch tip. In experiments, cracks were found occurring on the edge of the blister after the tungsten samples were exposed to deuteron plasma [23]. Besides, the destruction of blisters with erosion at the boundary was observed by SEM after the irradiation of deuterium ion fluence [41]. These observations confirm our simulated results. The thermal stress concentration in the current geometric structure can be explained with similar methods as in the former sections. Shown in Fig. 6b is the local temperature distribution of our model. It is obvious that a

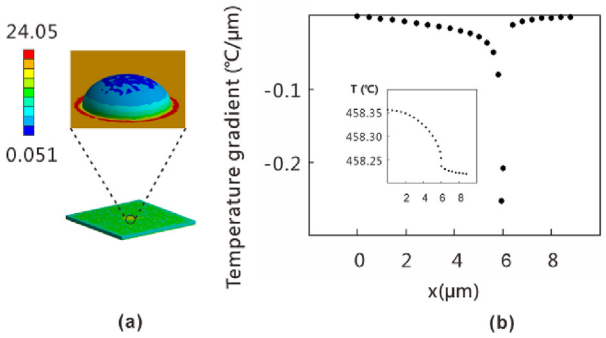

Fig. 6. (a) Calculated local distribution of the vMES around a bulged bubble as magnified from the whole simulation model. (b) Temperature distribution near the bubble boundary and its gradient.

large variation of the temperature gradient may develop in the intersection region surrounding the bubble, as one can observe from Fig. 6b. The highest temperature at the zenith of the bubble is due to the heat insulating character of the bubble, which accumulates heat from the plasma at its front surface. While the other parts of the tungsten tile have obviously much better heat conducting property and thus have a relatively lower temperature resulting in large temperature gradient in the intersection region (Fig. 6). Our simulations clearly indicate that the concentration phenomenon of vMES depends crucially on the location of the bubbles.

3.1.4. Effect of the bubble shape

In actual situations, the bubbles can take different shapes, which may result in different damages to the tungsten tiles. To see these differences, we have prepared three different models to simulate the effects of the shape (Fig. 7). The radius of the spheroid bubble (Fig. 7a) is set to be 5 μm, while the three semi-principal axes of the two ellipsoid bubbles (Fig. 7b and c) are chosen as $a = b = 5$ and $c = 3$ μm as well as $a = b = 3$ and $c = 5$ μm. Each bubble is put at the center of the xy plane of the model with their zenith at 0.01 μm below the surface. As can be seen from Fig. 7, the maximum value of the vMES in each case occurs at the top of the bubble and is calculated as 86.8, 61.9 and 43.4 MPa for the oblate ellipsoid, spheroid and prolate ellipsoid bubble, respectively. The stress concentration at the zenith of the bubble, as in the former section, can be well explained by using temperature gradient.

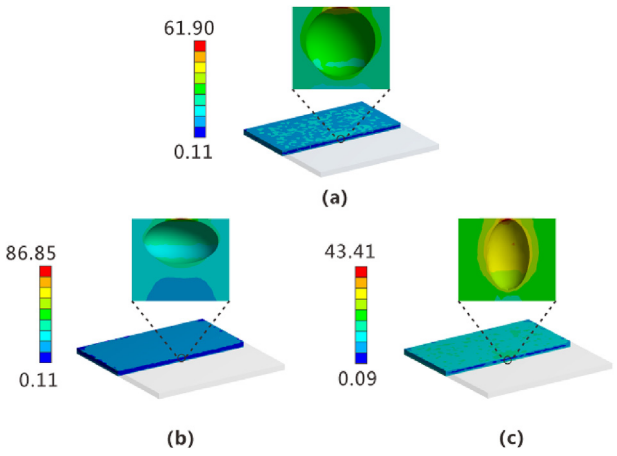

Fig. 7. Local distribution of the vMES around (a) a spheroid bubble, (b) an oblate ellipsoid bubble, and (c) a prolate ellipsoid bubble. The bubbles are magnified for clarity.

Shown in Fig. 8 are the temperature distributions along the x axis (see Fig. 1) for the three bubble shapes. Approximately a bubble can be considered as a heat-insulating object. Therefore, as one can see from Fig. 8, the oblate ellipsoid in its current dimension is the most heat insulating structure, while the spheroid is the second and the prolate ellipsoid is the last one. As a consequence, the temperature takes a maximum value around the zenith ($x = 0$, $y = 0$, $z = 1000$ mm) for the three bubble shapes. As the temperature distribution is very similar to that in Fig. 5b, the same argument follows for the order of the vMES of the three different bubble shapes.

3.1.5. The case of two bubbles

In the former sections, we have investigated the case of a single bubble, which itself represents an ideal situation or the cases of many bubbles which are sparsely distributed so that the interactions between them can be neglected. In actual situations, there can be many bubbles which may be densely distributed in the front wall material. In the following, we discuss the results simulated on the simplest two-bubble problem.

As a special case, we choose two identical round bubbles of the same size as in the former section ($r = 5$ μm). The dumbbell structure is made at 0.01 μm under the surface as that in section 3.1.4 with the z axis passing through the midpoint of the "dumbbell handle", which is parallel to the x axis and perpendicular to the y axis. To study the synergetic effects of the bubbles, we have simulated the problem with four different distances $d = 0.01$, 2.0, 5.0, 10.0 μm (the closest distance between the spheres). As shown in Fig. 9a, the local maximum values of the vMES field occur at two positions for each bubble, one at the inner-side point of the bubble while the other at the zenith. Our simulations indicate that the vMES at the zenith is larger than that at the side point for $d > 2.0$ μm. Within our simulation range, the vMES at the zenith, ~70 MPa, is larger than that of single bubble case (i.e., ~60 MPa). This difference obviously results from the increase in the heat insulating region caused by one extra bubble. As can be seen from Fig. 9b, the vMES at the side point will become larger than that at the zenith if the two bubbles approach each other ($d <$ ~2.0 μm). As the stress concentration in the current case is also caused by the heat loading on the tungsten tile, it can be explained by using temperature gradient analyses as used in the previous sections. The dominating vMES concentration at the side point implies that the wall between the bubbles can easily be perforated if the two bubbles are too close, a phenomenon already observed in experiments

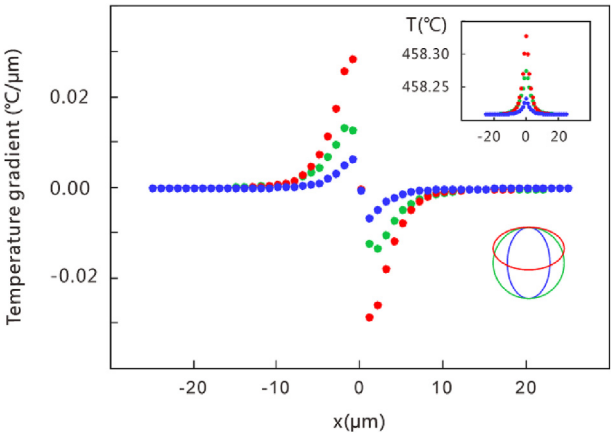

Fig. 8. Temperature distribution and its gradient along a line (x, $y = 0$, $z = 1000$) mm on the top of the three bubble models.

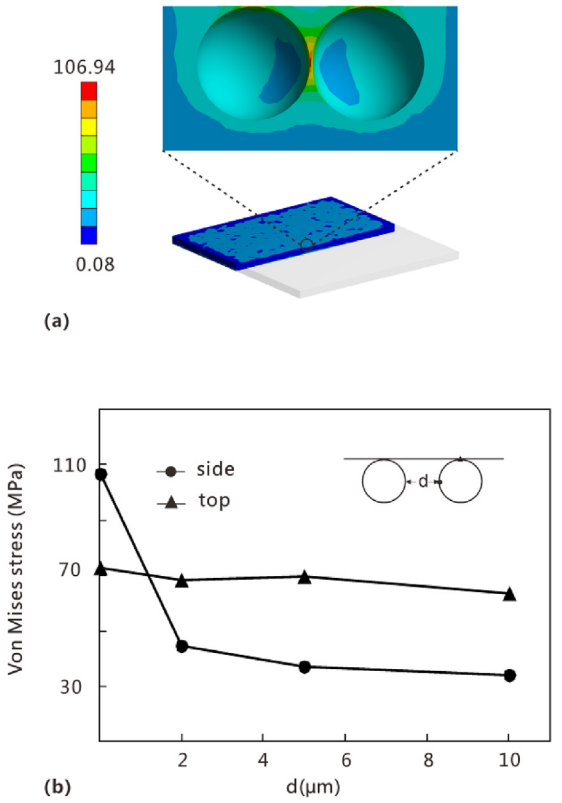

Fig. 9. (a) The calculated local vMES (in MPa) distribution around the two bubbles. (b) The dependence of vMES on the distance between the two inner side points of the bubbles.

wherein the hole or channel to the neighbor bubble were found at the bubble wall [42,43].

3.2. Transient heat loads

In addition to the steady state operation conditions, the ITER design must also consider the case of transient heat loads caused by plasma disruptions, vertical displacement events as well as edge localized modes, etc., in which the energy flux on the order of several GW/m^2 can be released within 1–10 ms [44,45] to the first wall material. In this work, we use the following exponential function [46] to describe the explosive energy release due to the plasma.

$$q_0 = 1000 \exp\left(-\frac{t}{0.00434}\right) \tag{16}$$

where t represents the time. As the transient heat loads normally occurs after a period of steady state operation, the initial temperature field is set to be that of the steady state temperature distribution for the corresponding models. Two models, one with a single round bubble as in section 3.1.4 and the other without any bubble, are chosen to do the simulations for the test of transient heat loads.

3.2.1. Peak temperature distribution and plastic deformation

The explosive energy release from the plasma causes a rapid temperature increase in the tungsten tiles, which may result in the failure of the first wall of the fusion chamber and leads to a catastrophic consequence. Given a dynamic heat source as described by Eq. (16), we have calculated the time dependent temperature field with the boundary conditions and initial conditions described above. As one can see from Fig. 10 a and b, the temperature distribution for the tungsten tile without bubble is more homogeneous than that with one bubble.

In addition, the arrival of peak temperature, ~2510 °C, for the bubbled case is ~1 ms earlier than the arrival of ~2400 °C of the no-bubble case. Our simulations indicate that at t = ~4 ms the peak temperature can be reached for the model with one bubble, where the maximum temperature occurs at the top of the bubble. Fig. 10c shows the time dependence of the temperature at (0, 0, 1000), a position slightly above the zenith of the bubble. As can be seen from Fig. 10c, though the half width of the temperature peak due to the transient heat loads is rather narrow (<~15 ms), the temperature value at the tail of the temperature peak (t = 0.1 s) is still ~1100°C, which is much higher than that of the maximum value of the temperature (~460°C) under steady state working condition (Figs. 5b and 6b). The temperature takes a maximum value at the top of a bubble for the same reason as explained in the previous sections. However, in the current case, this phenomenon becomes more pronounced, reducing the yield strength of the tungsten. According to the formula given in Table 1, the yield strength can be calculated as $\sigma_{ys}(2400\ ^\circ C) = 12.4$ MPa, $\sigma_{ys}(2500\ ^\circ C) = 10.2$ MPa. On the other hand, the vMES can be calculated at a specific time using the method described in section 2. Then one can judge whether a plastic deformation can occur or not by using the inequality Eq. (6). Our simulations indicate that the vMES far exceeds σ_{ys} at the peak temperature for both the one-bubble and no-bubble models. For example, the largest value of the vMES, σ_e, found on the mesh points for finite elements calculations is ~968.6 MPa and 705.4 MPa for the one-bubble and no-bubble model at the peak temperatures, respectively. Thus, a plastic behavior occurs in the events of transient heat loads. Shown in Fig. 11a and b are the calculated plastic strain for the no-bubble model and one-bubble model, respectively. It is obvious that the plastic strain in the one-bubble model is more inhomogeneous and larger than that in the no-bubble model. In particular, the plastic strain concentrates mainly around the bubble. The accumulation of such a plastic deformation due to the repeated transient heat loads may result in the cracks and finally the fracture of the tungsten near the head of the bubbles [24]. When the number of such bubbles increases, the amount of the exfoliated tungsten becomes considerable. The latter is a source of the high Z dust in the fusion chamber. In addition, with the local detachment of the tungsten around the bubble head, separated open cavities or coalesced bubbles can be formed between which thin walls or hair-

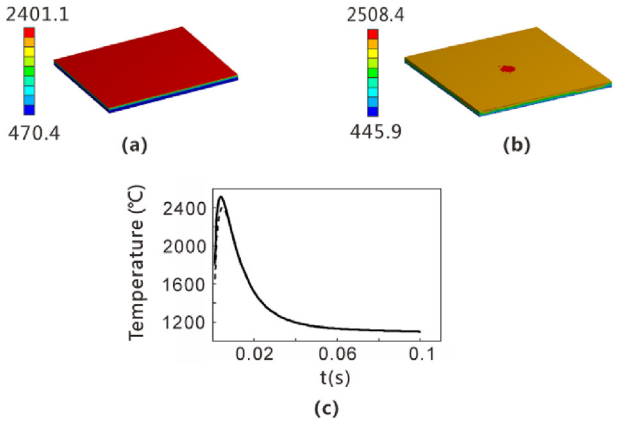

Fig. 10. (a) Temperature distribution for the model with no bubble. (b) Temperature distribution for the model with a single bubble. (c) The time dependence of the temperature at (0, 0, 1000) mm is shown as the dotted line for the model (a), and as the solid line for the model (b).

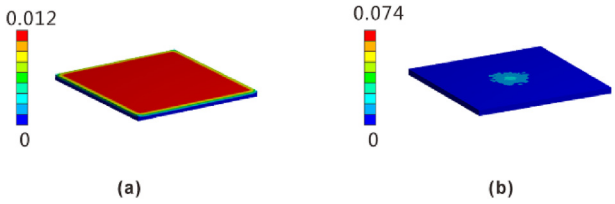

Fig. 11. The calculated distribution of the plastic strain on (a) the model without bubble and (b) the model with a single bubble.

like objects can be formed as already observed in some test experiments [13,23,47].

3.2.2. The optimal thickness of a tungsten tile

Taking into account the situations of strong transient heat loads, the thickness of the tungsten tile becomes a critical issue for the security of the fusion reactor. To solve this problem, one needs to find the peak temperature of the tungsten tile at various thicknesses. With the same model and conditions as the one shown in Fig. 10a, the simulations have been performed with five different thicknesses. A time step of 0.001 s is used for Eq. (16) to find the peak temperature. In Fig. 12, the calculated peak temperature versus the thickness is shown. The calculated data points can be well fitted with one branch of a shifted hyperbola as shown in Fig. 12. Our simulations indicate that when the thickness becomes smaller than 2 mm, the peak temperature rises very rapidly (catastrophe region), which sets a lower bound of the future design for the tungsten armor or tile. Of course, this bound depends on the magnitude of the transient heat loads and the cooling efficiency conditions, etc. The current standard of the ITER design [26] and of experimental models [48] is around 2 mm. However, if one considers the various possible damages such as that caused by Helium bubbles etc., a higher value should be used. An earlier Monte Carlo simulation [49] gave a value of 3 mm, which is consistent with our result. Fig. 12 indicates also that the peak temperature deviates considerably from the hyperbola curve when the thickness reaches ~50 mm. This is due to that the cooling efficiency of the setup decreases with increasing the thickness of the tungsten tile, a phenomenon also recognized by other researchers [50]. As can be seen from Fig. 12, the lower bound of the peak temperature should be larger than 2267°C, which far exceeds the temperature of a creep deformation for tungsten as estimated by $T_{creep} \approx T_m * 35\% \approx 1179°C$ [51]. This value becomes much smaller if shear stress exists. All these results indicate that the current design parameter of 2 mm for the tungsten armor or tile is too close to the catastrophe point.

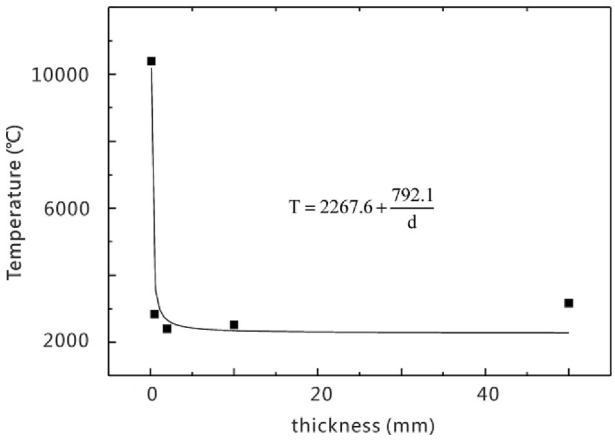

Fig. 12. The dependence of the simulated peak temperature on the thickness of the tungsten tile model without bubble.

4. Conclusions

In summary, the damage of the tungsten tile caused by the gas bubble has been evaluated by using the von Mises criterion. Starting from the definition of von Mises equivalent stress (vMES), a new relation between the extremal value of vMES field and that of the temperature field has been established for the case of unique heat load. In comparison with the non-damaged model, the bubble problem has been studied with respect to the bubble shape, location to the surface and the synergetic effect between the bubbles. The simulated vMES concentration is well explained using the calculated temperature field and its gradient. Under transient heat loads, plastic deformation has been found to occur and is significantly enhanced by the presence of the bubbles, and the lower bound of the security thickness of the tungsten tile is estimated to be greater than 2 mm. In all the studied cases, no plastic deformation has been found under steady operational conditions. Our simulations indicate that the bubbles near the tungsten surface are much more detrimental to the tungsten tile than those located deep inside the material. The predicted concentration locations of vMES agree well with the observed crack positions of the tungsten surface in many test experiments (i.e., the adjacent region of a bubble). Such results provide reasonable explanations for the observed pits and the rough or hairy surface morphology etc. Our simulations showed that the damage of the bubbles is not severe enough to lead to catastrophic failure of the tungsten armor, instead it is of local and gradual nature. There are more complicated situations, which include non-regular bubble shape, concave or non-smooth surface etc. as well as other loads such as the electromagnetic force, seismic situation etc. They should be considered together with the heat loads. We leave these issues to our future work.

Declaration of competing interest

The authors declare that they have no known competing financial interests or personal relationships that could have appeared to influence the work reported in this paper.

Acknowledgements

This work is financially supported by the National Natural Science Foundation (NSF) of China (21921001, 21703251, 61874122); the Strategic Priority Research Program of the Chinese Academy of Sciences (CAS) (XDB20000000); the National Key Research and Development Program of China (2016YFB0701001); the NSF of Fujian Province (2019J05151, 2019J01121); Youth Innovation Promotion of CAS (2019302); 100 Talents Program of CAS and Fujian Province.

References

[1] G. Janeschitz, I. Jct, HTs, Plasma-wall interaction issues in ITER, J. Nucl. Mater. 290 (2001) 1–11.
[2] H. Bolt, V. Barabash, W. Krauss, J. Linke, R. Neu, S. Suzuki, N. Yoshida, A.U. Team, Materials for the plasma-facing components of fusion reactors, J. Nucl. Mater. 329 (2004) 66–73.
[3] V.A. Chuyanov, ITER EDA project status, J. Nucl. Mater. 233 (1996) 4–8.
[4] A.A. Shoshin, A.S. Arakcheev, A.V. Arzhannikov, A.V. Burdakov, I.A. Ivanov, A.A. Kasatov, K.N. Kuklin, S.V. Polosatkin, V.V. Postupaev, S.L. Sinitsky, A.A. Vasilyev, L.N. Vyacheslavov, Study of plasma-surface interaction at the GOL-3 facility, Fusion Eng. Des. 114 (2017) 157–179.
[5] J.-C. Wang, W. Wang, R. Wei, X. Wang, Z. Sun, C. Xie, Q. Li, G.-N. Luo, Effect of Ti interlayer on the bonding quality of W and steel HIP joint, J. Nucl. Mater. 485 (2017) 8–14.

[6] Z.J. Bergstrom, M.A. Cusentino, B.D. Wirth, A molecular dynamics study of subsurface hydrogen-helium bubbles in tungsten, fusion, Sci. Technol. 71 (2017) 122–135.
[7] E. Bernard, R. Sakamoto, E. Hodille, A. Kreter, E. Autissier, M.F. Barthe, P. Desgardin, T. Schwarz-Selinger, V. Burwitz, S. Feuillastre, S. Garcia-Argote, G. Pieters, B. Rousseau, M. Ialovega, R. Bisson, F. Ghiorghiu, C. Corr, M. Thompson, R. Doerner, S. Markelj, H. Yamada, N. Yoshida, C. Grisolia, Tritium retention in W plasma-facing materials: impact of the material structure and helium irradiation, Nucl. Mater. Energy. 19 (2019) 403–410.
[8] S. Blondel, D.E. Bernholdt, K.D. Hammond, B.D. Wirth, Continuum-scale modeling of helium bubble bursting under plasma-exposed tungsten surfaces, Nucl. Fusion 58 (2018) 126034.
[9] X. Yang, W. Qiu, L. Chen, J. Tang, Tungsten–potassium: a promising plasma-facing material, Tungsten 1 (2019) 141–158.
[10] C. Linsmeier, M. Rieth, J. Aktaa, T. Chikada, A. Hoffmann, J. Hoffmann, A. Houben, H. Kurishita, X. Jin, M. Li, A. Litnovsky, S. Matsuo, A. von Müller, V. Nikolic, T. Palacios, R. Pippan, D. Qu, J. Reiser, J. Riesch, T. Shikama, R. Stieglitz, T. Weber, S. Wurster, J.H. You, Z. Zhou, Development of advanced high heat flux and plasma-facing materials, Nucl. Fusion 57 (2017), 092007.
[11] L. Wang, T. Hao, B.-L. Zhao, T. Zhang, Q.-F. Fang, C.-S. Liu, X.-P. Wang, L. Cao, Evolution behavior of helium bubbles and thermal desorption study in helium-charged tungsten film, J. Nucl. Mater. 508 (2018) 107–115.
[12] S.B. Gilliam, S.M. Gidcumb, N.R. Parikh, D.G. Forsythe, B.K. Patnaik, J.D. Hunn, L.L. Snead, G.P. Lamaze, Retention and surface blistering of helium irradiated tungsten as a first wall material, J. Nucl. Mater. 347 (2005) 289–297.
[13] G.N. Luo, K. Umstadter, W.M. Shu, W. Wampler, G.H. Lu, Behavior of tungsten with exposure to deuterium plasmas, Nucl. Instrum. Methods Phys. Res. B 267 (2009) 3041–3045.
[14] C.S. Becquart, C. Domain, Ab initio calculations about intrinsic point defects and He in W, Nucl. Instrum. Methods Phys. Res. B 255 (2007) 23–26.
[15] Y.-L. Liu, Y. Zhang, H.-B. Zhou, G.-H. Lu, F. Liu, G.N. Luo, Vacancy trapping mechanism for hydrogen bubble formation in metal, Phys. Rev. B 79 (2009) 172103.
[16] Y.-W. You, D. Li, X.-S. Kong, X. Wu, C.S. Liu, Q.F. Fang, B.C. Pan, J.L. Chen, G.N. Luo, Clustering of H and He, and their effects on vacancy evolution in tungsten in a fusion environment, Nucl. Fusion 54 (2014) 103007.
[17] K.O.E. Henriksson, K. Nordlund, J. Keinonen, D. Sundholm, M. Patzschke, Simulations of the initial stages of blistering in helium implanted tungsten, Phys. Scripta T108 (2004) 95–98.
[18] K.O.E. Henriksson, K. Nordlund, J. Keinonen, Molecular dynamics simulations of helium cluster formation in tungsten, Nucl. Instrum. Methods Phys. Res. B. 244 (2006) 377–391.
[19] N. Juslin, B.D. Wirth, Interatomic potentials for simulation of He bubble formation in W, J. Nucl. Mater. 432 (2013) 61–66.
[20] N. Enomoto, S. Muto, T. Tanabe, J.W. Davis, A.A. Haasz, Grazing-incidence electron microscopy of surface blisters in single- and polycrystalline tungsten formed by H+, D+ and He+ irradiation, J. Nucl. Mater. 385 (2009) 606–614.
[21] J.-H. You, Mechanics of tungsten blistering: a finite element study, J. Nucl. Mater. 437 (2013) 24–28.
[22] M. Li, J.-H. You, Mechanics of tungsten blistering II: analytical treatment and fracture mechanical assessment, J. Nucl. Mater. 465 (2015) 702–709.
[23] Y.Z. Jia, W. Liu, B. Xu, G.N. Luo, C. Li, S.L. Qu, T.W. Morgan, G. De Temmerman, Thermal shock behaviour of blisters on W surface during combined steady-state/pulsed plasma loading, Nucl. Fusion 55 (2015) 113015.
[24] H. Guo, M. Xia, Q. Yan, L. Guo, J. Chen, C. Ge, Microstructure of medium energy and high density helium ion implanted tungsten, Acta Phys. Sin. 65 (2016), 077803.
[25] S.V. Patankar, Numerical Heat Transfer and Fluid Flow, Hemisphere Publishing Corporation, Washington DC, 1980.
[26] K. Tomabechi, J.R. Gilleland, Y.A. Sokolov, R. Toschi, Iter conceptual design, Nucl. Fusion 31 (1991) 1135–1224.
[27] P. Zhang, J. Zhao, Y. Qin, B. Wen, Numerical simulation of the combined effects of plasma heating and neutron heating loads on the ITER first wall, Fusion Eng. Des. 86 (2011) 45–50.
[28] W.D. Pilkey, D.F. Pilkey, Peterson's Stress Concentration Factors, 3rd rev. edn. ed., Springer, New York, 2008.
[29] J.F. Nye, Physical Properties of Crystals, Oxford University Press, London, 1967.
[30] Y. Wang, S. Liang, P. Xiao, J. Zou, FEM simulations of tensile deformation and fracture analysis for CuW alloys at mesoscopic level, Comput. Mater. Sci. 50 (2011) 3450–3454.
[31] J.W. Davis, P.D. Smith, ITER material properties handbook, J. Nucl. Mater. 233 (1996) 1593–1596.
[32] M. Bhuyan, S.R. Mohanty, C.V.S. Rao, P.A. Rayjada, P.M. Raole, Plasma focus assisted damage studies on tungsten, Appl. Surf. Sci. 264 (2013) 674–680.
[33] M.J. Inestrosa-Izurieta, E. Ramos-Moore, L. Soto, Morphological and structural effects on tungsten targets produced by fusion plasma pulses from a table top plasma focus, Nucl. Fusion 55 (2015), 093011.
[34] J. Schijve, Fatigue of Structures and Materials, second ed., Springer, New York, 2009.
[35] W.M. Shu, E. Wakai, T. Yamanishi, Blister bursting and deuterium bursting release from tungsten exposed to high fluences of high flux and low energy deuterium plasma, Nucl. Fusion 47 (2007) 201–209.
[36] S. Kajita, W. Sakaguchi, N. Ohno, N. Yoshida, T. Saeki, Formation process of tungsten nanostructure by the exposure to helium plasma under fusion relevant plasma conditions, Nucl. Fusion 49 (2009), 095005.
[37] Y.Z. Jia, W. Liu, B. Xu, G.N. Luo, C. Li, B.Q. Fu, G. De Temmerman, Nano-structures and pinholes on W surfaces exposed to high flux D plasma at high temperatures, J. Nucl. Mater. 463 (2015) 312–315.
[38] Y. Ding, C. Ma, M. Li, Q. Hou, Molecular dynamics study on the interactions between helium projectiles and helium bubbles pre-existing in tungsten surfaces, Nucl. Instrum. Methods Phys. Res. B. 368 (2016) 50–59.
[39] J. Cui, Z. Wu, Q. Hou, Estimation of the lifetime of small helium bubbles near tungsten surfaces – a methodological study, Nucl. Instrum. Methods Phys. Res. B. 383 (2016) 136–142.
[40] B.L. Zhang, J. Wang, M. Li, Q. Hou, A molecular dynamics study of helium bubble formation and gas release near titanium surfaces, J. Nucl. Mater. 438 (2013) 178–182.
[41] J. Song, N.-K. Kim, H.-S. Kim, Y. Jin, K.-B. Roh, G.-H. Kim, Deuterium ion irradiation induced blister formation and destruction, Fusion Eng. Des. 109–111 (2016) 624–628.
[42] D. Nishijima, M.Y. Ye, N. Ohno, S. Takamura, Formation mechanism of bubbles and holes on tungsten surface with low-energy and high-flux helium plasma irradiation in NAGDIS-II, J. Nucl. Mater. 329 (2004) 1029–1033.
[43] A.A. Airapetov, L.B. Begrambekov, I.Y. Gretskaya, A.V. Grunin, M.Y. Dyachenko, N.A. Puntakov, Y.A. Sadovskiy, Thermal cycling and high power density hydrogen ion beam irradiation of tungsten layers on tungsten substrate, J. Phys. Conf. Ser. 748 (2016), 012009.
[44] T. Hirai, K. Ezato, P. Majerus, ITER relevant high heat flux testing on plasma facing surfaces, Mater. Trans. 46 (2005) 412–424.
[45] G. Federici, C.H. Skinner, J.N. Brooks, J.P. Coad, C. Grisolia, A.A. Haasz, A. Hassanein, V. Philipps, C.S. Pitcher, J. Roth, W.R. Wampler, D.G. Whyte, Plasma-material interactions in current tokamaks and their implications for next step fusion reactors, Nucl. Fusion 41 (2001), 1967-2137.
[46] S. Huang, Y. Zhao, W. Wang, Numerical evaluation on heat shock resistance of two ITER-like first wall mockups, J. Fusion Energy 34 (2015) 1465–1477.
[47] M.J. Baldwin, R.P. Doerner, Formation of helium induced nanostructure 'fuzz' on various tungsten grades, J. Nucl. Mater. 404 (2010) 165–173.
[48] N.P. Taylor, R. Pampin, Activation properties of tungsten as a first wall protection in fusion power plants, Fusion Eng. Des. 81 (2006) 1333–1338.
[49] Y. Igitkhanov, B. Bazylev, Evaluation of energy and particle impact on the plasma facing components in DEMO, Fusion Eng. Des. 87 (2012) 520–524.
[50] S. Sharafat, N.M. Ghoniem, M. Anderson, B. Williams, J. Blanchard, L. Snead, Micro-engineered first wall tungsten armor for high average power laser fusion energy systems, J. Nucl. Mater. 347 (2005) 217–243.
[51] M.F. Ashby, H. Shercliff, D. Cebon, Materials: Engineering, Science, Processing and Design, Elsevier, Oxford, 2014.